

Pansharpening: Context-Based Generalized Laplacian Pyramids by Robust Regression

Gemine Vivone¹, Senior Member, IEEE, Stefano Marano², Senior Member, IEEE,
and Jocelyn Chanussot³, Fellow, IEEE

Abstract—Pansharpening refers to the combination of panchromatic (PAN) and multispectral (MS) images, designed to obtain a fused product retaining the fine spatial resolution of the former and the high spectral content of the latter. One of the most popular and successful approaches to pansharpening is the method known as context-based generalized Laplacian pyramid, which requires as a key ingredient for the estimation of the so-called injection coefficients. In this article, we propose the adoption of robust techniques for the estimation of the injection coefficients and detection strategies to select the clusters for which robust regression is needed, providing a suitable balancing between fusion performance and computational burden. Experimental results conducted on five real data sets acquired by the sensors QuickBird, WorldView-3, and WorldView-4, show the superiority of the proposed method with respect to current state-of-the-art pansharpening techniques.

Index Terms—Clustering, image fusion, multiresolution analysis (MRA), pansharpening, remote sensing, robust regression.

I. INTRODUCTION

EVERY DAY SATELLITE sensors acquire a huge amount of data and exploiting them to address several human tasks. Thus, there exists an increasing interest in data-fusion techniques that are able to coherently combine satellite data. The need of high spatial resolution multispectral (MS) images, which cannot be acquired by a unique device because of physical constraints [1], has driven forward the development of methods that are able to combine high spatial but low spectral resolution images (usually panchromatic, henceforth PAN) with MS images, which are characterized by opposite spatio-spectral features. These methods are named “pansharpening,” which stands for PAN sharpening, i.e., the enhancement of the spatial resolution of an MS image achieved through a PAN image.

The scientific interest about pansharpening is widely discussed in thousands of journal articles, several surveys [1]–[4], and comprehensive books [5] published in the past few years.

Manuscript received September 17, 2019; revised January 9, 2020; accepted February 14, 2020. Date of publication March 4, 2020; date of current version August 28, 2020. (Corresponding author: Gemine Vivone.)

Gemine Vivone and Stefano Marano are with the Department of Information Engineering, Electrical Engineering and Applied Mathematics, University of Salerno, 84084 Fisciano, Italy (e-mail: gvivone@unisa.it; marano@unisa.it).

Jocelyn Chanussot is with LJK, CNRS, Grenoble INP, Inria, Université Grenoble Alpes, 38000 Grenoble, France (e-mail: jocelyn.chanussot@gipsa-lab.grenoble-inp.fr).

Color versions of one or more of the figures in this article are available online at <http://ieeexplore.ieee.org>.

Digital Object Identifier 10.1109/TGRS.2020.2974806

We also mention the specific data fusion context organized by the IEEE Data Fusion Committee of the IEEE Geoscience and Remote Sensing Society [6]. Pansharpening also has an important impact on our everyday life as witnesses, e.g., by the massive use of pansharpened images by popular software like Google Earth.

A. Background and Related Works

Pansharpening methods can be classified into three main classes. The first class is named component substitution (CS), which refers to methods that perform a substitution of a component to enhance the spatial resolution of an MS image. In particular, first, a forward transformation is implemented to isolate the spatial component of the MS image, which usually is referred to as the intensity component. Then, the intensity component is replaced by a PAN image in order to obtain the desired enhancement of the spatial component. Examples of methods belonging to this class include: the Brovey transform [7], the intensity-hue-saturation transform [7], [8], the Gram–Schmidt (GS) spectral sharpening [9], the GS adaptive (GSA) approach [10], the partial replacement adaptive CS (PRACS) method [11], and the band-dependent spatial detail (BDSD) approach [12].

The second class is based on the concept of multiresolution analysis (MRA). This class of methods consists in the decomposition of the PAN image to extract its high-resolution components (image “details”) to be injected into the MS data. Popular multiresolution frameworks exploited to this aim include the “à-trous” wavelet transforms [13] and the discrete wavelet transforms [14]. The MRA is computationally demanding but recent studies revealed that a whole decomposition of the PAN image is not necessary, suggesting the use of simple low-pass spatial filters suitably designed by exploiting *a priori* information about the acquisition device [15]. Instances of MRA-based approaches belonging to this class are: the smoothing filter-based intensity modulation (SFIM) approach [1], [16]; the additive à-trous wavelet transform (ATWT) technique [13], [17]; the additive wavelet luminance proportional (AWLP) method [18], [19]; the generalized Laplacian pyramid (GLP) [14] using the MS sensor’s modulation transfer function (MTF)-matched filters with projective [6], [20], additive [17], or high pass modulation injection schemes [21]; approaches based on nonlinear filters [22]; and deconvolution frameworks designed to extract image details without any *a priori* information [23].

For both the CS and MRA approaches, the adoption of context-based techniques has been advocated to ensure high performance thanks to the ability to adapt the fusion rule to specific portions of the images [24]–[27].

The third class of pansharpening methods relies on the concept of superresolution or, more generally, variational optimization. Model-based implementations have been proposed [28], [29]. Furthermore, convolutional neural networks have recently been exploited for PAN sharpening [30]–[33]. Approaches belonging to the third class of pansharpening methods include: Bayesian methods [34], variational approaches [28], [29], [35], and compressed sensing techniques [36]–[39]. Despite their formal mathematical elegance, superresolution approaches provide only incremental performance improvements with respect to the state-of-the-art methods of CS and MRA [40]. Such an improvement comes at the cost of high computational burden [41] and the presence of many parameters to be tuned [29], which explains why CS and MRA are nowadays commonly advocated for both benchmarking and practical uses.

B. Contribution

Context-based MRA approaches, which relied upon the GLP designed to match the MS sensor’s MTF, show state-of-the-art performance [27]. This article elaborates on this framework and is aimed at providing a further improvement over the state-of-the-art performance when the illuminated scene is nonhomogeneous in the spectral domain.

More specifically, the most powerful context-based GLP implementations employ linear regression to estimate the injection coefficients [1]. Here, we argue that the regression-based approaches may be inappropriate in fusing MS and PAN data when the residuals of the ordinary least-squares (OLS) used to estimate the injection coefficients do not follow a Gaussian distribution, which is typically assumed at the design stage. Significant deviations from Gaussianity usually arise when the vegetated area is involved. In these situations, we advocate the use of robust regression approaches that relied upon the *M-estimation* framework pioneered by Huber [42]. We mention in passing that robust regression has also been recently advocated in fusing eight-band data sets using the BDSD approach [43].

The drawback of the use of robust regression is the computational cost required for the estimation task, which is a critical aspect in context-adaptive approaches. In order to alleviate the computational burden, we propose the adoption of *k*-means clustering algorithm to partition the acquired scene in spectrally homogeneous clusters, followed by cluster detection techniques to identify those clusters for which robust estimation of the injection coefficients is expected to provide meaningful performance improvements. We consider two strategies for cluster selection. The first exploits semantic properties of the cluster (i.e., it is based on normalized difference indexes), while the other one relies upon the analysis of the residuals of the least-squares (LS) estimator.

Injection coefficients for clusters not selected by the above procedure are obtained by the standard LS estimation. Instead, coefficients for clusters selected by the above procedure are

obtained by a robust estimation procedure. Two robust regressions are proposed in this article. The first is based on the concept of outlier removal, where the outliers are identified by analyzing the statistical distribution of the OLS procedure. After removing the outliers, an LS estimator is implemented on the surviving data. The second method relies upon the bisquare robust regression.

The cluster selection and robust estimation algorithms are integrated into the state-of-the-art GLP fusion framework, to sharpen each cluster of the MS image using the PAN image. The proposed approach is tested on five data sets acquired by three different sensors (i.e., QuickBird (QB), WorldView-3, and WorldView-4). Performance assessment is conducted both at reduced resolution [44], and at full resolution (FR) exploiting proper quality indexes without reference [45]. The performance and computational burden of the proposed method are then compared to that of several state-of-the-art methods, used as the benchmark.

C. Notation and Organization

We use bold lowercase letters to denote vectors (e.g., \mathbf{x}) and bold uppercase to denote matrices (e.g., \mathbf{X}). A monochromatic image is represented by lexicographic ordering its pixels, namely by stacking their columns into a vector. Thus, $\mathbf{p} \in \mathbb{R}^N$ denotes the PAN image consisting of N pixels. Accordingly, MS images are organized in a matrix form in which each column corresponds to a spectral band. $\mathbf{M} \in \mathbb{R}^{N/R^2 \times B}$ is the observed MS image, where B is the number of bands and R is the spatial resolution ratio between the MS and the PAN images. The MS image upsampled to the PAN scale is denoted by $\tilde{\mathbf{M}} \in \mathbb{R}^{N \times B}$, and the pansharpened image is denoted by $\hat{\mathbf{M}} \in \mathbb{R}^{N \times B}$. The b th band of an MS image \mathbf{X} is denoted by \mathbf{x}_b . The generic multidimensional pixel n (sampling the spectral signature according to the MS spectral response) of \mathbf{X} is denoted by \mathbf{x}^n . Finally, the generic pixel n of the monochromatic PAN image is denoted by p^n .

The rest of this article is arranged as follows. Section II presents the adopted notation and a classification of the pansharpening approaches. In Section III, the OLS and the proposed robust regression approaches applied to the GLP are described. The context-based robust GLP methods are detailed in Section IV together with the strategies to select clusters in which a robust regression is needed. The experimental results are shown in Section V. Finally, a summary is offered in Section VI.

II. REVIEW OF PANSHARPENING METHODS

This section is devoted to the presentation of the two main classes of pansharpening methods, i.e., CS and MRA [1].

A. Component Substitution

Approaches belonging to the CS family are based on the concept of substitution of a component to sharpen the MS image. In particular, first a forward transformation on the MS image is performed in order to isolate its spatial component. Then, this component is substituted with the

PAN image (possibly equalized) in order to obtain the higher spatial resolution. Finally, a backward transformation gives the desired pansharpened product. If the transformation is linear and a single component is substituted, this process can be summarized by the following fusion rule [1], [8]:

$$\hat{\mathbf{m}}_b = \tilde{\mathbf{m}}_b + g_b(\mathbf{p} - \mathbf{i}) \quad (1)$$

where $\hat{\mathbf{m}}_b$ is the fused product at band b , $\tilde{\mathbf{m}}_b$ is the upsampled version of the original MS image at band b , g_b is the injection coefficient for band b , and \mathbf{i} , often called intensity component, is defined as

$$\mathbf{i} = \sum_{b=1}^B w_b \tilde{\mathbf{m}}_b \quad (2)$$

where the weights $\{w_b\}_{b=1}^B$ are usually estimated by multivariate linear regression [10]. Both $\{w_b\}_{b=1}^B$ and $\{g_b\}_{b=1}^B$ depend on the particular transformation which they refer to [1]. Peculiarities of the approaches belonging to this category are the good rendering (i.e., a limited spatial distortion) and the modest computational burden. These advantages come at the cost of usually high spectral distortions of the outcomes.

B. Multiresolution Analysis

Early implementations of MRA pansharpening were based on MRA, two prominent examples of which are the “à-trous” wavelet transforms [13] and the discrete wavelet transforms [14]. In these methods, the PAN image is decomposed into elementary components, in order to extract the so-called PAN details (high-resolution features) to be injected into the MS image. Recently, it has been shown that the same state-of-the-art performance of the most sophisticated MRA approaches can be obtained by processing the PAN image by means of simple low-pass spatial filters, properly designed to match the MS sensor’s MTF [15]. In this case, the fusion rule can be cast as

$$\hat{\mathbf{m}}_b = \tilde{\mathbf{m}}_b + g_b(\mathbf{p} - \mathbf{p}_{LP}) \quad (3)$$

where \mathbf{p}_{LP} is the low-pass filtered version of the PAN image obtained through spatial filtering, and g_b represents the injection coefficient for band b . Despite the formal analogy between (1) and (3) the two methods give outcomes with completely different characteristics. Typically, the fused products obtained by MRA approaches are spectrally coherent but exhibit a higher spatial distortion with respect to the CS approaches.

MRA methods differ from each other by the way to calculate \mathbf{p}_{LP} and estimate $\{g_b\}_{b=1}^B$. State-of-the-art methods are based on GLP, matching the filters with the MS sensor’s MTFs in order to extract the PAN details (see [46]). These approaches will be on the basis of the methods described in Section III.

III. REGRESSION-BASED GLP APPROACHES

We now introduce the regression-based approaches for the estimation of the injection coefficients, combining the general framework of the *M-estimators* [42] and the state-of-the-art GLP method for detail extraction. The OLS regression and

two robust regression techniques based on the removal of outliers (RO) and the bisquare weighted LS will be detailed in the forthcoming sections. First, the GLP fusion method is formalized.

A. Fusion Problem Formulation

For each band $b \in \{1, \dots, B\}$, the GLP fusion rule is shown in (3). Implementation of (3) requires the design of the low-pass filters, which defines \mathbf{p}_{LP} and the estimation of g_b . As to the latter, recalling that $\hat{\mathbf{m}}$ (the result of the pansharpening algorithm) is unknown, a reference image playing its role is needed. Following [6] and [46], a possible solution is to exploit the original low-resolution MS image $\tilde{\mathbf{m}}$ as surrogate of $\hat{\mathbf{m}}$. This approach relies upon the assumption of “invariance among scales” for the estimated coefficients. This means that the coefficients estimated at reduced resolution are used as they are to *inject* the details at full PAN resolution.

To elaborate, let us rewrite (3) in a compact form as

$$\mathbf{y}_b = g_b \mathbf{d} \quad (4)$$

where $\mathbf{y}_b = \hat{\mathbf{m}}_b - \tilde{\mathbf{m}}_b$ and $\mathbf{d} = \mathbf{p} - \mathbf{p}_{LP}$. Let us denote by \mathbf{d}_r the reduced spatial resolution counterpart of \mathbf{d} and by $\mathbf{y}_{b,r}$ the corresponding counterpart of \mathbf{y}_b . These quantities are obtained through low-pass filters matched with the sensors’ MTFs with a cutoff frequency $1/R$. From (4) we have

$$\mathbf{y}_{b,r} = g_b \mathbf{d}_r \quad (5)$$

where $\mathbf{y}_{b,r} = \tilde{\mathbf{m}}_b - \tilde{\mathbf{m}}_{b,LP}$, $\mathbf{d}_r = \mathbf{p}_{LP} - \mathbf{p}_{LP,LP}$, $\tilde{\mathbf{m}}_{b,LP}$ is the low spatial resolution version of $\tilde{\mathbf{m}}_b$, and $\mathbf{p}_{LP,LP}$ is the low-pass resolution version of \mathbf{p}_{LP} obtained by using an MTF-based filter with cutoff frequency $1/R^2$.

In the next sections, we describe several approaches to solve the overdetermined linear system (5), which provides the desired estimate of g_b to be used in (3).

B. GLP With *M*-Estimators

A general approach to solve (5) with respect to g_b is the *M-estimation* procedure pioneered by Huber [42]. To explain this approach, let us refer to a generic pixel n , that is

$$y_{b,r}^n = g_b d_r^n. \quad (6)$$

The *M-estimator* of g_b is the value that minimizes the following objective function:

$$\sum_{n=1}^N \rho(y_{b,r}^n - g_b d_r^n) \quad (7)$$

where ρ is a function to be specified later. This yields

$$\hat{g}_b = \arg \min_{g_b} \sum_{n=1}^N \rho(y_{b,r}^n - g_b d_r^n). \quad (8)$$

Differentiating (7) with respect to g_b and setting the partial derivatives to zero, we have

$$\sum_{n=1}^N \psi(y_{b,r}^n - g_b d_r^n) d_r^n = 0 \quad (9)$$

Algorithm 1 Iterative Weighted Least-Squares

Data: The degraded vectors \mathbf{d}_r and $\mathbf{y}_{b,r}$; the weighting function w_b^n ; the threshold for the convergence, T ; the maximum number of iterations, T_{\max} .

Result: The estimated injection coefficient g_b .

begin

- Select the initial (at step 0) estimate, $\hat{g}_b^{(0)}$, using a least-squares approach, i.e.,

$$\hat{g}_b^{(0)} = [\mathbf{d}_r^T \mathbf{d}_r]^{-1} \mathbf{d}_r^T \mathbf{y}_{b,r} \quad (12)$$

- Set $t = 0$, $C^{(0)} = +\infty$

while $t \leq T_{\max}$ and $C^{(t)} > T$ **do**

- $t = t + 1$

- Calculate residuals $e_b^{n,(t-1)} = y_{b,r}^n - d_r^n \hat{g}_b^{(t-1)}$ and the associated weights $w_b^{n,(t-1)}$ for each pixel $n \in \{1, \dots, N\}$ using the coefficients $\hat{g}_b^{(t-1)}$

- Solve the weighted least-squares as in (11), i.e.,

$$\hat{g}_b^{(t)} = [\mathbf{d}_r^T \mathbf{W}_b^{(t-1)} \mathbf{d}_r]^{-1} \mathbf{d}_r^T \mathbf{W}_b^{(t-1)} \mathbf{y}_{b,r}, \quad (13)$$

where $\mathbf{W}_b^{(t-1)} = \text{diag}(w_b^{n,(t-1)})$ and $\text{diag}(\cdot)$ denotes a diagonal matrix

- $C^{(t)} = |\hat{g}_b^{(t)} - \hat{g}_b^{(t-1)}|$

end

- $g_b = \hat{g}_b^{(t)}$

end

where ψ is the derivative of ρ . Defining the weighting function as

$$w_b^n = w(y_{b,r}^n - g_b d_r^n) = \frac{\psi(y_{b,r}^n - g_b d_r^n)}{y_{b,r}^n - g_b d_r^n}. \quad (10)$$

We see that (9) can be recast in the form of a *weighted LS problem*, as follows:

$$\sum_{n=1}^N w_b^n [y_{b,r}^n - g_b d_r^n] d_r^n = 0. \quad (11)$$

Algorithm 1 provides an iterative solution to (11). The parameters T and T_{\max} are empirically set to 10^{-6} and 50, respectively.

Different definitions of ρ lead to different estimators. In the forthcoming sections, we explore some of the common definitions, showing a tradeoff between performance and computational burden. Henceforth, we denote the residual for band b and pixel n by $e_b^n = y_{b,r}^n - g_b d_r^n$.

1) *GLP With Least-Squares*: In the case of the OLS, function ρ is defined as [42]

$$\rho(e_b^n) = (e_b^n)^2 \quad (14)$$

i.e., the goal is to minimize the mean square error, and the weighting function w_b^n reduces to a constant. Since step 0 of Algorithm 1 returns just the minimum mean square estimator,

for this choice of ρ Algorithm 1 is applied with $T_{\max} = -1$, (i.e., no iterations are required).

When the residuals $\{e_b^n\}_{n=1}^N$ follow a Gaussian distribution, the OLS estimator coincides with the maximum likelihood one [47]. Suboptimal performance (in the maximum-likelihood sense) is instead expected when the residuals have heavy-tailed distributions. One reason for the appearance of distributions with tails heavier than those of the Gaussian is the presence of outliers, here informally defined as samples that significantly deviate from the distribution of the large majority of the data. Accordingly, the first solution to address the non-Gaussianity of the residuals consists in the identification and RO. This solution implies only modest computational burdens, and it is explored in Section III-B2. A second approach, which is more elaborated and more computationally demanding, relies upon the use of a fitting criterion that is less vulnerable to outliers with respect to OLS. This is presented in Section III-B3.

2) *GLP With RO*: The simplest way to identify the outliers is to consider very low or very high values of residuals [42]. Cast in the general framework of the *M-estimation*, this amounts to adopt the following expression for the function ρ introduced in (7):

$$\rho(e_b^n) = \begin{cases} (e_b^n)^2, & \text{if } C_l < e_b^n < C_u \\ (C_l)^2, & \text{if } e_b^n \leq C_l, \\ (C_u)^2, & \text{otherwise} \end{cases} \quad (15)$$

where the parameters $C_l < C_u$ are threshold values to be suitably set by the designer. The resulting weighting function is

$$w_b^n = \begin{cases} 2, & \text{if } C_l < e_b^n < C_u \\ 0, & \text{otherwise.} \end{cases} \quad (16)$$

The estimator can be computed by exploiting Algorithm 1, as follows: 1) T_{\max} is set to 0; 2) $w_b^{n,(0)}$ is given by (16) wherein e_b^n is replaced by the residuals of the OLS $e_b^{n,(0)} = y_{b,r}^n - d_r^n \hat{g}_b^{(0)}$; and 3) the parameters C_l and C_u are set to two percentiles of the residuals calculated after step 0 (OLS).

3) *GLP With Bisquare Regression (BR)*: For the bisquare robust regression, the function ρ introduced in (7) takes the form [42]

$$\rho(e_b^n) = \begin{cases} \frac{C_T^2}{6}, & \text{if } |e_b^n| > C_T \\ \frac{C_T^2}{6} \left\{ 1 - \left[1 - \left(\frac{e_b^n}{C_T} \right)^2 \right]^3 \right\}, & \text{otherwise} \end{cases} \quad (17)$$

for a suitable choice of the parameter C_T . The corresponding weighting function becomes

$$w_b^n = \begin{cases} 0, & \text{if } |e_b^n| > C_T \\ \left[1 - \left(\frac{e_b^n}{C_T} \right)^2 \right]^2, & \text{otherwise.} \end{cases} \quad (18)$$

The tuning parameter C_T is of great importance. Small values of C_T give more resistance to outliers, but at the expense of lower efficiency if residuals are normally distributed. Following [48], C_T is set to $\xi \hat{\sigma}$, where $\hat{\sigma}$ is an estimate of

the standard deviation of the errors and ζ is empirically set according to the analysis developed in Section V. A robust measure of the spread $\hat{\sigma}$ is $\text{MAD}/0.6745$ [48], where MAD is the median absolute deviation of the residuals computed at step 0 of Algorithm 1.

IV. CONTEXT-BASED GLPS WITH ROBUST REGRESSION

In this section, the proposed fusion framework will be detailed. First, the k -means clustering is presented. Afterward, the critical issue of selecting the clusters in which a robust regression has to be applied will be considered, to guarantee both high performance and an affordable computational burden. Finally, the complete fusion algorithm will be described.

A. k -Means Clustering

The clustering method is applied to the upsampled MS image, as suggested in [27]. One of the most popular and widely used clustering methods is known as k -means (or Lloyd's algorithm), which is an iterative procedure based on an initial set of k random means (at step 0), denoted by $\mu^{1,(0)}, \dots, \mu^{k,(0)}$. The algorithm proceeds by assigning each pixel of the upsampled MS image $\tilde{\mathbf{M}}$ to the j th cluster whose mean, $\mu^{j,(0)}$, has the least-squared Euclidean distance from the pixel. Then, the calculation of the new means (centroids) is performed. The algorithm iteratively proceeds until the pixel assignment to clusters does not change significantly anymore. The procedure is detailed in Algorithm 2. The parameters T^c and T_{\max}^c are empirically set to 10^{-6} and 100, respectively.

B. Detection of Clusters Requiring Robust Analysis

This section is devoted to the presentation of three approaches to detect clusters that need to undergo a robust analysis. This is a crucial step in order to get high performance with a limited computational burden. The first approach is semantic-based and relies upon the calculation of the normalized difference vegetation index (NDVI). The other two are based on the analysis of residuals arising from the OLS regression.

1) *Semantic-Based Selection*: The semantic-based selection relies upon the calculation of an index that is related to the nature of the pixels in the generic i th cluster \mathcal{S}^i . The rationale behind the approach is that the simpler OLS estimator may not be able to guarantee high performance for clusters characterized by a predominance of vegetated areas. This is due to the fact that the distribution of the OLS residuals in the rural/vegetated areas typically deviates significantly from the Gaussian, as exemplified in Fig. 1. In these circumstances, the adoption of more robust estimators is desirable. Therefore, different clusters are classified in terms of their NDVI index, whose computation requires an estimation of the reflectance starting from the acquired data. Accordingly, the following three-step procedure is implemented.

- 1) A radiometric calibration of $\tilde{\mathbf{m}}^n = [\tilde{m}_1^n, \dots, \tilde{m}_b^n, \dots, \tilde{m}_B^n]$ for each $n \in \mathcal{S}^i$ is performed according to the indications provided by the data producer (usually, a linear model is exploited with sensor- and band-dependent

Algorithm 2 k -Means Clustering

Data: The upsampled MS image, $\tilde{\mathbf{M}}$; the number of clusters, k ; the threshold for the convergence, T^c ; the maximum number of iterations, T_{\max}^c .

Result: The clustered pixels, $\{\mathcal{S}\}_{j=1}^k$.

begin

- Draw the initial (at step 0) k random means,

$\mu^{1,(0)}, \dots, \mu^{k,(0)}$

- $t = 0$, $C^{(0)} = +\infty$

while $t \leq T_{\max}^c$ and $C^{(t)} > T^c$ **do**

- $t = t + 1$

for $n \in \{1, \dots, N\}$ **do**

- $j = -1$, $\delta^n = +\infty$

for $i \in \{1, \dots, k\}$ **do**

- $\delta^{n,i} = \|\tilde{\mathbf{m}}^n - \mu^{i,(t-1)}\|^2$

if $\delta^{n,i} \leq \delta^n$ **then**

- $\delta^n = \delta^{n,i}$

- $j = i$

end

end

- $\mathcal{S}^{j,(t)} = \mathcal{S}^{j,(t-1)} \cup \{n\}$

end

for $i \in \{1, \dots, k\}$ **do**

- $\mu^{i,(t)} = \frac{1}{|\mathcal{S}^{i,(t)}|} \sum_{n \in \mathcal{S}^{i,(t)}} \tilde{\mathbf{m}}^n$, where $|\cdot|$ indicates the number of elements in $\mathcal{S}^{i,(t)}$

end

- $C^{(t)} = \sum_{i=1}^k \|\mu^{i,(t)} - \mu^{i,(t-1)}\|$

end

end

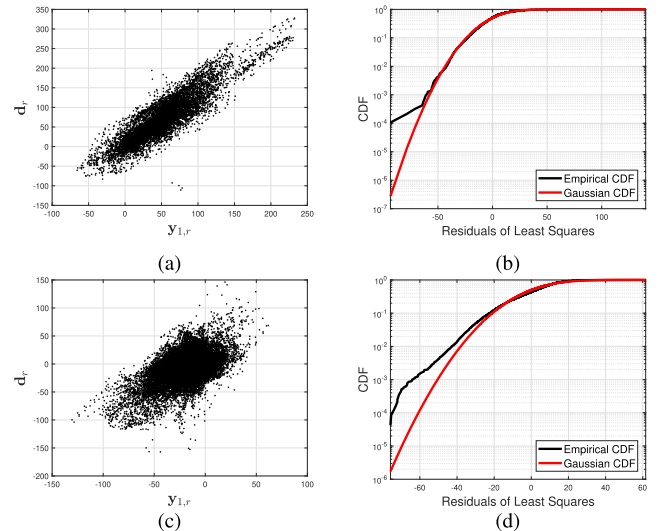


Fig. 1. Band 1 (blue) of the QB Trento data set. (Left) Scatter plots of $y_{1,r}$ and d_r . (Right) Empirical cumulative distribution function (CDF) for the OLS residuals. (Top) Urban-area cluster with NDVI= 0.2441. (Bottom) Vegetated cluster with NDVI= 0.7855. Note that the larger the NDVI is, the worse the Gaussian fit is.

gains and offsets) in order to get an estimation of at-sensor radiance for the multidimensional pixel $\tilde{\mathbf{m}}^n$.

- 2) Afterward, the compensation of the atmospheric effects is performed. In particular, the path radiance for each spectral band of $\tilde{\mathbf{m}}^n$ is removed by exploiting dark object subtraction (DOS) techniques [49], [50]. Thus, we have an at-sensor radiance only accounting for the unscattered component (neglecting secondary diffusion effects) of the radiation model [51], denoted by $\mathbf{l}^n = [l_1^n, \dots, l_b^n, \dots, l_B^n]$.
- 3) Finally, the reflectance of $\tilde{\mathbf{m}}^n$ at band b , i.e., \tilde{m}_b^n , can be estimated by the following expression:

$$\rho(\tilde{m}_b^n) = \frac{\pi l_b^n d_{\text{ES}}^2}{E_b \cos(\theta_s)} \quad (19)$$

where d_{ES} is the Earth–Sun distance in astronomical unit, E_b is the solar exoatmospheric irradiance at band b , and θ_s is the solar zenith angle [51].

In order to calculate the NDVI, the red and the near-infrared (NIR) spectral bands are used. Let b_1 and b_2 be the indexes that refer to these bands, we have

$$\text{NDVI} = \frac{\rho(\tilde{m}_{b_2}^n) - \rho(\tilde{m}_{b_1}^n)}{\rho(\tilde{m}_{b_2}^n) + \rho(\tilde{m}_{b_1}^n)}. \quad (20)$$

The NDVI for cluster i is obtained by averaging all the NDVIs, calculated as in (20), for all the multidimensional pixels belonging to set \mathcal{S}^i . If this value is greater than 0.5, the area in the cluster i is considered vegetated and then we assume that a robust regression is required. The threshold value 0.5 follows by experimental results, as detailed in Section V-D. Formally, we introduce the set function $f(\cdot)$ such that $f(\mathcal{S}^i) = 1$ if a robust regression is required, and $f(\mathcal{S}^i) = 0$ otherwise.

2) *Selection Based on Analysis of Residuals*: The other two approaches to detect clusters that need a robust regression are based on the analysis of the OLS residuals. In particular, for each $n \in \mathcal{S}^i$, the OLS residuals for a given spectral band b , say $e_b^n = y_{b,r}^n - d_r^n g_b$, (where g_b is the OLS estimation of the injection coefficient using all the pixels $n \in \mathcal{S}^i$), are calculated. The vector of the residuals is denoted by $\mathbf{e}_b^{\mathcal{S}^i}$. Two metrics are considered to quantify the deviation from normality.

- 1) The first one is the *skewness*, which measures the asymmetry of the probability distribution of a random variable about its mean. This index is defined as [52]

$$\gamma_b^i = \frac{\mathbb{E}\left\{\left[\mathbf{e}_b^{\mathcal{S}^i} - \mathbb{E}(\mathbf{e}_b^{\mathcal{S}^i})\right]^3\right\}}{\left(\mathbb{E}\left\{\left[\mathbf{e}_b^{\mathcal{S}^i} - \mathbb{E}(\mathbf{e}_b^{\mathcal{S}^i})\right]^2\right\}\right)^{3/2}} \quad (21)$$

where $\mathbb{E}[\cdot]$ indicates the expectation operator. Of course, in our experiments, the expectation operator is approximated by its empirical counterpart. By averaging $\{\gamma_b^i\}_{b=1}^B$ along the spectral dimension, we get

$$\gamma^i = \frac{1}{B} \sum_{b=1}^B \gamma_b^i. \quad (22)$$

If γ^i is greater than a threshold (set to 0.18 in the experiments of Section V-D), the distribution of the residuals is considered asymmetric and, thus, not Gaussian, implying the use of robust regression.

- 2) The second index is the *kurtosis*, which measures the tailedness of the probability distribution of a random variable. In formula [52]

$$\beta_b^i = \frac{\mathbb{E}\left\{\left[\mathbf{e}_b^{\mathcal{S}^i} - \mathbb{E}(\mathbf{e}_b^{\mathcal{S}^i})\right]^4\right\}}{\left(\mathbb{E}\left\{\left[\mathbf{e}_b^{\mathcal{S}^i} - \mathbb{E}(\mathbf{e}_b^{\mathcal{S}^i})\right]^2\right\}\right)^2}. \quad (23)$$

By averaging $\{\beta_b^i\}_{b=1}^B$ along the spectral dimension, we have

$$\beta^i = \frac{1}{B} \sum_{b=1}^B \beta_b^i. \quad (24)$$

If β^i is greater than a threshold (empirically set to 1.5, see Section V-D), the distribution of the residuals is considered non-Gaussian, implying the use of robust regression.

C. Proposed Fusion Framework

The whole fusion framework is now dealt with in detail. First, a clustering based on the k -means algorithm is performed, see Section IV-A, where the number k of clusters to be identified is decided beforehand. In order to identify which of the k clusters need a robust regression approach to estimate the injection coefficients, one of the criteria discussed in Section IV-B is adopted. The total number of clusters selected to be handled by robust regression is denoted by $q \leq k$. Afterward, the estimation (*robust* or *classical*) of the injection coefficients is performed according to the GLP-based approaches discussed in Section III. Finally, exploiting these estimates, for each cluster, the data fusion is realized according to (3). Algorithm 3 summarizes the proposed context-based robust regression GLP approach.

V. EXPERIMENTAL RESULTS

This section is devoted to the assessment of the performance and computational burden of the proposed pansharpening algorithms. As to the performance assessment, two procedures are applied. The first is conducted at a reduced resolution following Wald's protocol [44], according to which the MS image and the PAN image are spatially degraded to get a reference image, i.e., the original (not spatially degraded) MS image, usually called ground truth (GT). The second performance assessment procedure is accomplished at FR, i.e., it exploits indexes working at the highest (PAN) resolution. The latter assessment is less accurate than the former, but working at the PAN spatial resolution implies some advantage, as discussed in [45]. In summary, each assessment has its own pros and cons, and the experimental analysis is more reliable when both validations are considered.

In Sections V-A–V-F, we first describe the data sets used in the experimentation. Afterward, some state-of-the-art pansharpening methods used as performance benchmarks are presented. Then, the similarity indexes for comparing MS images are detailed. Finally, we present the results of the proposed pansharpening approach both at reduced resolution and at FR, along with the analysis of the computational burden.

Algorithm 3 Context-Based Robust Regression GLP Fusion

Data: The upsampled MS image, $\tilde{\mathbf{M}}$; the PAN image, \mathbf{p} ; the low-pass filtered PAN image, \mathbf{p}_{LP} ; the number of clusters, k ; the set function $f(\cdot)$ labeling clusters that need robust analysis.

Result: The pansharpened image $\tilde{\mathbf{M}}$.

begin

- Cluster $\tilde{\mathbf{M}}$ in k clusters according to Algorithm 2 to

get $\{\mathcal{S}^i\}_{i=1}^k$

for $i \in \{1, \dots, k\}$ **do**

if $f(\mathcal{S}^i)$ is 1 **then**

 - Estimate $\{g_b\}_{b=1}^B$ according to a robust estimator, see Sects. III-B2 or III-B3

else

 - Estimate $\{g_b\}_{b=1}^B$ according to the OLS estimator, see Sect. III-B1

end

for $n \in \mathcal{S}^i$ **do**

for $b \in \{1, \dots, B\}$ **do**

$$\hat{m}_b^n = \tilde{m}_b^n + g_b(p^n - p_{LP}^n) \quad (25)$$

end

end

end

end

A. Data Sets

In this section, the three exploited datasets will be described.

- 1) *WorldView-3 Rio Data Set:* A WorldView-3 (WV-3) image has been acquired over the urban area of Rio, Brazil. The WV-3 satellite sensor acquires eight MS bands in the visible NIR spectrum (i.e., coastal, blue, green, yellow, red, red edge, NIR1, and NIR2). The spatial resolution is about 1.2 m. A PAN image is also captured at a higher spatial resolution of about 0.3 m. The scale ratio between the PAN and the MS images is $R = 4$. The radiometric resolution of both the images amounts to 11 bits. This data set is exploited for the performance assessment at reduced resolution. The GT and the low spatial resolution MS images are shown in Fig. 2(a) and (d), respectively. Note that the size of the PAN image is 512×512 pixels.
- 2) *QB Trento Data Set:* A QB image has been acquired over the city of Trento, Italy. The QB satellite sensor acquires four MS bands in the visible NIR spectrum (i.e., blue, green, red, and NIR). The spatial resolution is 2.44 m at nadir. A PAN image is also captured at a higher spatial resolution of 0.61 m. As for the previous case, $R = 4$ and the radiometric resolution is 11 bits. This data set is exploited for both the assessments: 1) at reduced resolution, where the size of the PAN image is 256×256 pixels and 2) at FR, where the size of the PAN image is 1024×1024 pixels. The GT and the low spatial resolution MS images are shown in Fig. 2(b) and (e), respectively.

- 3) *WorldView-4 Alice Data Set:* A WorldView-4 (WV-4) image has been acquired over the rural area of Alice Springs, Australia. The WV-4 satellite sensor acquires four MS bands in the visible NIR spectrum (i.e., blue, green, red, and NIR). The spatial resolution is 1.24 m at nadir. A PAN image is also captured at a spatial resolution of 0.31 m. Again, $R = 4$ and the radiometric resolution of the involved data is 11 bits. This data set is exploited for both the assessments at reduced and at FR, where the size of the PAN image is 1024×1024 pixels. The GT and the low spatial resolution MS images are shown in Fig. 2(c) and (f), respectively.

B. Benchmarks

In order to compare the results of the proposed method to those of the state-of-the-art method, we refer to the following recently proposed pansharpening approaches as benchmarks. Furthermore, the MS image interpolation using a polynomial kernel with 23 coefficients (EXP) [14], [53] is included as a yardstick.

The CS benchmarks are: the BDDSD technique [12] and its context-based generalization, denoted by C-BDDSD, with ten clusters [26], the GS method [9], the GSA technique [10] and its context-based version, called C-GSA, with three clusters [27], and the PRACS method [11].

The benchmarks belonging to the MRA class are: the SFIM approach [1], [16], the ATWT technique [13], [17], the additive wavelet luminance proportional (AWLP) method [18], [19], the GLP [14] using the MS sensor's MTF-matched filters with context-based decision (GLP-CBD) [6], the GLP using the full scale (FS) regression-based injection model (GLP-FS) [20], and the morphological (MF) half gradient using the high pass modulation injection scheme (MF) [22]. For comparison purposes, we also include as a benchmark the GLP-LS, which is a context-based GLP MTF-based approach using a k -means for clustering the MS data and an LS estimator to solve (5) [27].

The proposed pansharpening approaches are denoted by GLP-RO, when the estimation of the injection coefficients is performed by the RO technique, and GLP-BR, when the BR method is used. Both these approaches are used in conjunction with the strategies described in Section IV-B to select the clusters for which the robust regression is implemented: 1) NDVI indicates the use of the NDVI index calculated on the upsampled MS image; 2) β denotes the method based on the kurtosis; and 3) γ denotes the adoption of the skewness-based strategy.

C. Quality Indexes

The performance assessment at reduced resolution is simply performed by comparing the fused product with the GT image. The adopted indexes account for the MS nature of the data to be compared. In particular, three similarity indexes are exploited to this aim. The overall quality index $Q2^n$ [54], [55] ($Q4$ or $Q8$ for four or eight bands, respectively) represents the MS extension of the universal image quality index proposed in [56]. This perceptual index takes into account both the radiometric and the spectral distortions. The implementation is

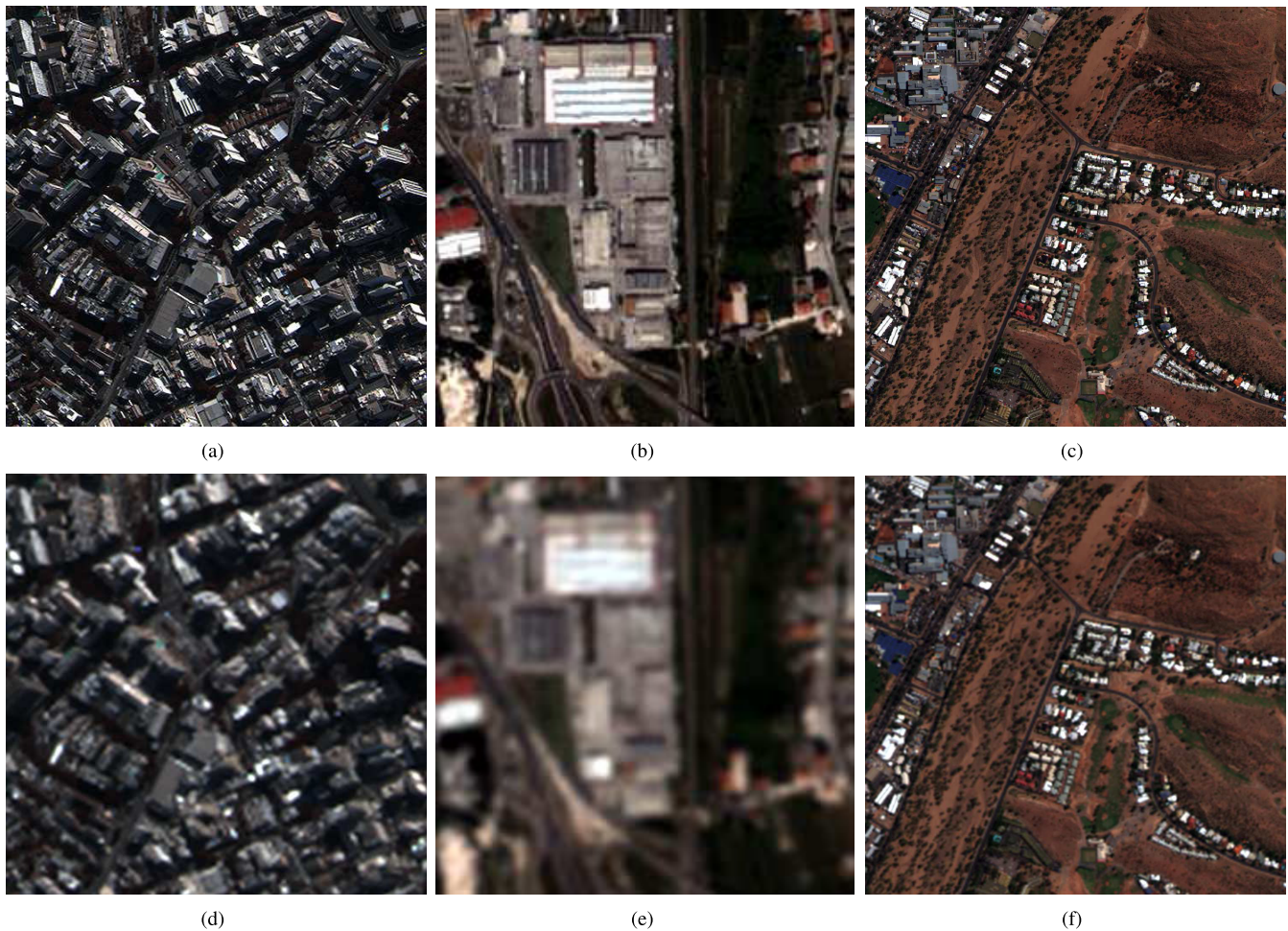


Fig. 2. Data sets (selected bands: red, green, and blue). (Top) GT images. (a) WorldView-3 Rio. (b) QB Trento. (c) WorldView-4 Alice. Bottom panels show the corresponding low spatial resolution MS images. (d) WorldView-3 Rio. (e) QB Trento. (f) WorldView-4 Alice.

block-based with a block size equal to 32. It takes values in the range $[-1, 1]$, and the optimal value is 1. The second index is the MS extension of the root mean square error (RMSE) called “erreur relative globale adimensionnelle de synthèse” (ERGAS) [1], [6]. It takes nonnegative values with zero being the best. The third index is the spectral angle mapper (SAM) [1], [57], which measures only the spectral distortion and measured in degrees. As for ERGAS, it can assume nonnegative values, with zero being the optimum.

Regarding the quality assessment at FR, many indexes have been proposed in the literature (see [45], [58]). In this article, the state-of-the-art hybrid quality with no reference (HQNR) index is exploited [45]. This is similar to the QNR index [58], with the modification that the spectral distortion D_i is measured by the spectral consistency property introduced by Wald *et al.* [44]. The implementation is block-based with a block size equal to 32. The HQNR assumes an optimal value equal to 1.

D. Reduced Resolution Performance Assessment

In this section, we describe the results obtained at reduced resolution, i.e., where a GT image is available. The implementation of the proposed pansharpening procedure requires

to set the values of several parameters that are under the control of the designer: k , which is the number of clusters for the k -means clustering, ζ , required for the implementation of BR, and the two thresholds C_l and C_u for the RO. To set these parameters, we have conducted extensive analyses over different data sets acquired by different sensors, over a wide variety of landscapes. Space limitations prevent us from presenting exhaustively these studies, and we limit to report a few examples of the analysis, yielding the final choice of the design parameters.

In Fig. 3(a), we show the overall quality index $Q2^n$ pertaining to the three reduced-resolution data sets, for the GLP-BR algorithm with $\zeta = 1$. It is seen that the choice of k is not critical for the data sets WV-4 Alice and WV-3 Rio. On the contrary, for the QB data set, good performance is obtained only with $k \geq 3$, which suggests the choice $k = 3$ in order to maintain the computational burden at an acceptable level. Furthermore, k equal to 3 is a common choice for clustering remotely sensed images. Indeed, three classes can be sufficient in order to split the man-made structures, vegetated areas, and water bodies. As we have already seen in Fig. 1, vegetated areas require the use of robust regression justifying the use of at least three classes. Finally, $k = 3$ enables us to have

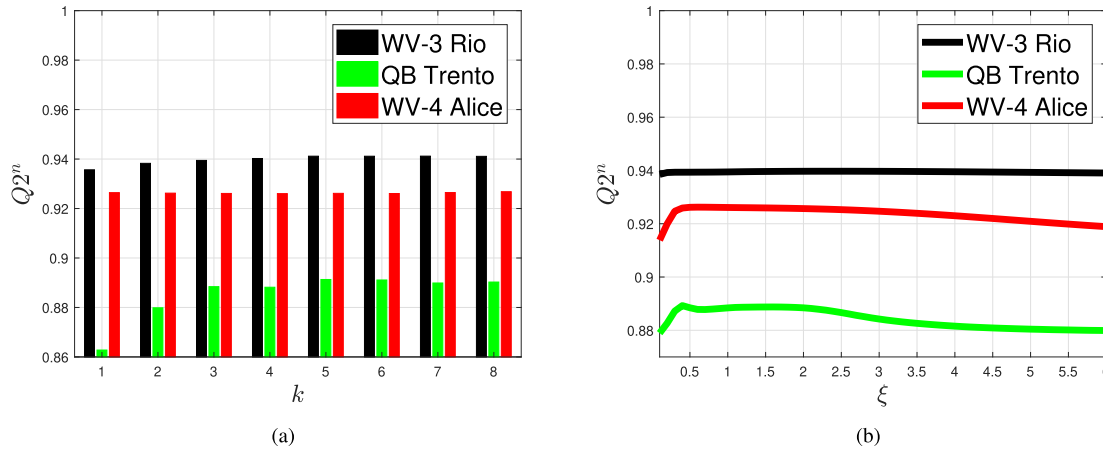


Fig. 3. Performance analysis based on $Q2^n$ index using BR regression, for the three reduced resolution data sets. (a) Number of clusters k , with $\xi = 1$. (b) Multiplicative coefficient ξ , with $k = 3$.

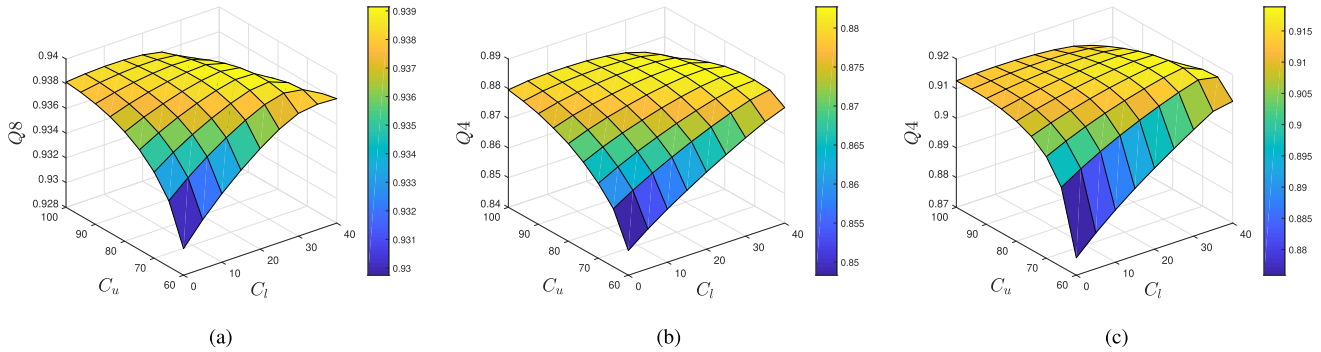


Fig. 4. Performance analysis based on $Q2^n$ index using RO regression, for the three reduced resolution data sets, in function of C_l and C_u . The data sets are (a) WV-3 Rio, (b) QB Trento, and (c) WV-4 Alice.

TABLE I
INDEXES NDVI, β , AND γ , FOR THE THREE REDUCED RESOLUTION DATA SETS AND THE DIFFERENT CLUSTERS

	WV-3 Rio			QB Trento			WV-4 Alice		
cluster id	1	2	3	1	2	3	1	2	3
NDVI	0.2300	0.2195	0.0752	0.3903	0.7855	0.2441	0.5898	0.6156	0.4519
β	3.0958	2.6158	2.2113	0.8758	0.2389	1.5286	3.8552	4.3570	0.7196
γ	0.6266	0.5647	0.3858	0.0770	0.3754	0.2861	0.1890	0.5520	0.0950

TABLE II
PERFORMANCE INDEX $Q4/Q8$ FOR DIFFERENT NUMBER $q \leq k$ OF CLUSTERS HANDLED BY ROBUST REGRESSION, WITH k , THE NUMBER OF CLUSTERS OF THE k -MEANS CLUSTERING, EQUAL TO 3, FOR THE THREE REDUCED RESOLUTION DATA SETS AND THE TWO PROPOSED ROBUST REGRESSION APPROACHES (RO AND BR) APPLIED TO THE GLP METHOD. BEST OVERALL RESULTS ARE SHOWN IN BOLDFACE, AND BEST RESULTS FOR EACH CLUSTER SELECTION METHOD (NDVI, β , γ) ARE UNDERLINED

		WV-3 Rio				QB Trento				WV-4 Alice			
	q	0	1	2	3	0	1	2	3	0	1	2	3
RO	NDVI	0.9381	0.9379	<u>0.9392</u>	0.9391	0.8790	<u>0.8808</u>	0.8806	0.8807	0.9111	0.9143	0.9177	0.9177
	β	0.9381	0.9379	<u>0.9392</u>	0.9391	0.8790	<u>0.8790</u>	0.8789	<u>0.8807</u>	0.9111	0.9143	<u>0.9177</u>	0.9177
	γ	0.9381	0.9379	<u>0.9392</u>	0.9391	0.8790	<u>0.8808</u>	0.8808	0.8807	0.9111	0.9143	<u>0.9177</u>	0.9177
BR	NDVI	0.9381	0.9373	<u>0.9397</u>	0.9395	0.8790	<u>0.8893</u>	0.8885	0.8884	0.9111	0.9184	<u>0.9261</u>	<u>0.9261</u>
	β	0.9381	0.9373	<u>0.9397</u>	0.9395	0.8790	<u>0.8789</u>	0.8781	0.8884	0.9111	0.9184	<u>0.9261</u>	<u>0.9261</u>
	γ	0.9381	0.9373	<u>0.9397</u>	0.9395	0.8790	<u>0.8893</u>	<u>0.8893</u>	0.8884	0.9111	0.9184	<u>0.9261</u>	<u>0.9261</u>

stable results strongly reducing the randomness of the k -means clustering approach exploited in our fusion framework.

With $k = 3$, Fig. 3(b) explores the effect of different values of ξ , and we see that $\xi = 1$ is a reasonable choice,

TABLE III
 PERFORMANCE INDEXES (Q_4/Q_8 , SAM MEASURED IN DEGREES, AND ERGAS) COMPUTED FOR THE THREE REDUCED RESOLUTION DATA SETS, USING THE FOLLOWING DESIGN PARAMETERS: $k = 3$, NDVI-THRESHOLD SET TO 0.5, β -THRESHOLD SET TO 1.5, AND γ -THRESHOLD SET TO 0.18. BEST OVERALL RESULTS ARE SHOWN IN BOLDFACE, AND BEST RESULTS FOR EACH CLUSTER SELECTION METHOD (NDVI, β , γ) ARE UNDERLINED

		WV-3 Rio			QB Trento			WV-4 Alice			
	regression	cluster selection	Q_8	SAM [°]	ERGAS	Q_4	SAM [°]	ERGAS	Q_4	SAM [°]	ERGAS
	EXP		0.6808	7.8062	10.3549	0.7803	3.3808	3.6751	0.7922	3.0519	4.0212
	BDS		0.9280	7.5242	5.4411	0.8612	3.6870	2.9791	0.8992	3.2758	2.8884
	GS		0.8650	7.8480	6.7224	0.7640	5.1560	3.9425	0.8655	3.1654	3.2138
	GSA		0.9364	6.8365	4.9036	0.8313	4.2280	3.3193	0.9031	3.2862	2.8063
	PRACS		0.9143	7.4560	5.6822	0.8546	3.6699	2.9285	0.9145	3.2437	2.7406
	SFIM		0.9016	6.9760	5.9083	0.8403	3.8700	260.6221	0.9139	3.0292	2.7019
	ATWT		0.9312	6.7654	5.0755	0.8387	3.7062	3.2176	0.9125	3.0411	2.6805
	AWLP		0.9312	7.3586	5.1895	0.8577	3.4545	3.1067	0.9164	3.4929	2.9116
	GLP-FS		0.9371	6.7647	4.8625	0.8497	3.9718	3.0311	0.9063	3.3115	2.7985
	GLP-CBD		0.9357	6.7864	4.9092	0.8471	4.0700	3.0653	0.9087	3.3076	2.7424
	C-GSA		0.9247	7.9110	5.8189	0.8763	3.2547	2.8851	0.9044	3.7646	2.9938
	C-BDS		0.9267	7.7479	5.6601	0.8752	3.7559	3.0005	0.9206	3.1950	2.8673
	MF		0.9188	6.8485	5.5650	0.8381	4.1132	3.8093	0.9139	3.0461	2.8491
GLP	LS		0.9381	7.0779	4.9323	0.8790	3.6910	2.8198	0.9111	3.3121	2.7512
		NDVI	0.9381	7.0779	4.9323	<u>0.8808</u>	3.6404	2.8011	<u>0.9177</u>	<u>3.1737</u>	<u>2.7083</u>
		β	0.9391	6.9078	4.8589	0.8790	3.6900	2.8183	0.9177	3.1737	2.7083
	RO	γ	<u>0.9391</u>	<u>6.9078</u>	<u>4.8589</u>	<u>0.8808</u>	<u>3.6393</u>	<u>2.7997</u>	<u>0.9177</u>	<u>3.1737</u>	<u>2.7083</u>
		NDVI	0.9381	7.0779	4.9323	0.8893	3.2996	2.7144	0.9261	2.9666	2.6719
		β	0.9395	6.7274	4.8184	0.8789	3.6787	2.8113	0.9261	2.9666	2.6719
		γ	0.9395	6.7274	4.8184	0.8893	<u>3.2875</u>	2.7057	0.9261	2.9666	2.6719

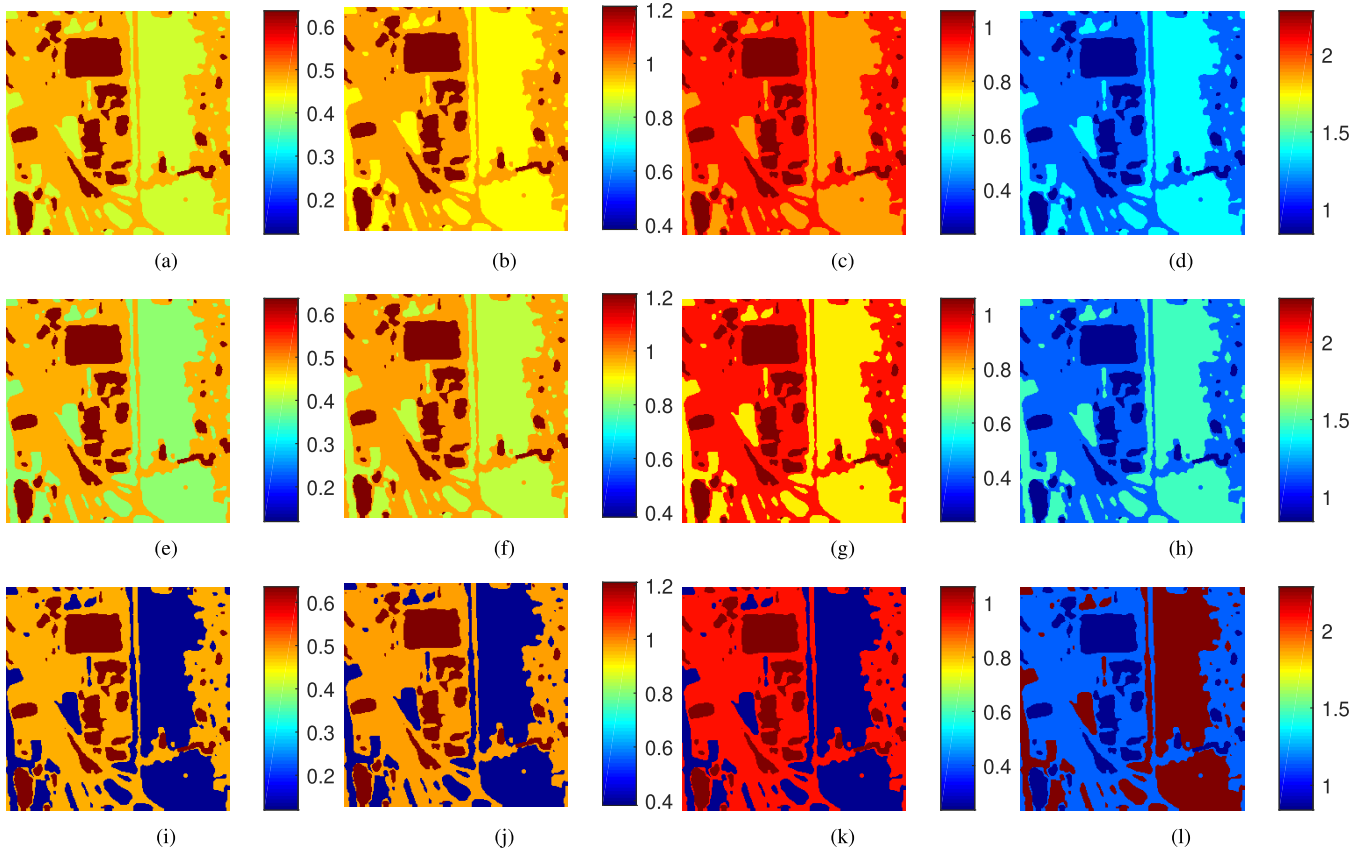


Fig. 5. Injection coefficients $\{g_b\}_{b=1}^B$ for the reduced resolution QB Trento data set. (a)–(d) GLP-LS. (e)–(h) GLP-RO. (i)–(l) GLP-BR using the NDVI cluster selection strategy. (Left to right) Coefficients for the blue, the green, the red, and the NIR bands.

namely, we henceforth assume $C_T = MAD/0.6745$ (see Section III-B3). One remark about the WV-3 Rio data set, indicated by the black line in Fig. 3(b), is its performance does not vary with ζ . This is because the WV-3 Rio data set does



Fig. 6. Close-ups of the fusion results for the reduced resolution QB Trento data set (selected bands: red, green, and blue). (a) GT. (b) EXP. (c) BSDS. (d) GS. (e) GSA. (f) PRACS. (g) SFIM. (h) ATWT. (i) AWLP. (j) GLP-CBD. (k) C-GSA. (l) C-BDS. (m) MF. (n) GLP-LS. (o) GLP-RO NDVI. (p) GLP-BR NDVI.

not require the use of robust estimation, as we will see later in Table III, making the choice of ζ immaterial and reducing the pansharpeing method to the GLP-LS.

Finally, let us consider the two thresholds C_l and C_u relevant to the GLP-RO method. Fig. 4 shows the $Q2^n$ -performance for each of the three data sets in function of C_l and C_u . Again, it can be seen that the performance in the case of the WV-3 Rio data set weakly depends on the choice of the two thresholds. In general, for all data sets close-to-best performance is attained with $C_l = 30$ (i.e., the 30th percentile) and $C_u = 80$ (80th percentile), and these values of the parameters are assumed henceforth.

Consider now the problem of selecting how many and which clusters need to undergo a robust estimation procedure. Again, we offer some representative examples of the conducted experiments. For each cluster, Table I reports the values of NDVI and spectral averaged skewness and kurtosis. Table II shows the performance obtained with a different number, q , of clusters undergoing the robust estimation procedure, where the specific clusters are selected on the basis of the metrics (NDVI, β , or γ) shown in Table I. Thus, in Table II the columns labeled with **0** refer to the use of the OLS estimator for all the $k = 3$ clusters. Likewise, the columns labeled with **1** refer to the case in which one of the $k = 3$ clusters

TABLE IV

PERFORMANCE INDEXES COMPUTED FOR THE TWO FR DATA SETS, USING THE FOLLOWING DESIGN PARAMETERS: $k = 3$, NDVI-THRESHOLD SET TO 0.5, β -THRESHOLD SET TO 1.5, AND γ -THRESHOLD SET TO 0.18. BEST OVERALL RESULTS ARE SHOWN IN BOLDFACE, AND BEST RESULTS FOR EACH CLUSTER SELECTION METHOD (NDVI, β , γ) ARE UNDERLINED

	regression	cluster selection	QB Trento FR			WV-4 Alice FR			
			D_λ	D_S	HQNR	D_λ	D_S	HQNR	
EXP			0.0503	0.1069	0.8482	0.0173	0.0580	0.9256	
BDS			0.0658	0.1322	0.8107	0.0307	0.0408	0.9297	
GS			0.1406	0.2220	0.6686	0.0367	0.0466	0.9184	
GSA			0.0921	0.2087	0.7184	0.0294	0.0781	0.8948	
PRACS			0.0574	0.0734	0.8734	0.0241	0.0562	0.9210	
SFIM			0.0608	0.1022	0.8433	0.0127	0.0352	0.9526	
ATWT			0.0624	0.1682	0.7798	0.0105	0.0523	0.9378	
AWLP			0.0603	0.1358	0.8121	0.0106	0.0429	0.9470	
GLP-FS			0.0576	0.1426	0.8080	0.0108	0.0537	0.9361	
GLP-CBD			0.0574	0.1424	0.8084	0.0108	0.0527	0.9370	
C-GSA			0.0744	0.1373	0.7985	0.0304	0.0762	0.8956	
C-BDS			0.0650	0.0734	0.8664	0.0303	0.0368	0.9340	
MF			0.0984	0.1678	0.7503	0.0131	0.0562	0.9314	
GLP	LS		0.0564	0.0578	0.8891	0.0107	0.0383	0.9514	
		RO	NDVI	0.0564	0.0578	0.8891	0.0107	0.0383	0.9514
			β	0.0550	0.0524	0.8954	0.0107	0.0376	0.9521
	γ		0.0550	0.0524	0.8954	0.0107	0.0376	0.9521	
	BR	NDVI	0.0529	0.0497	0.9000	0.0107	0.0383	0.9514	
		β	0.0530	0.0515	0.8982	0.0112	0.0354	0.9539	
		γ	0.0530	0.0515	0.8982	0.0112	0.0354	0.9539	

uses robust estimation (either RO or BR), and this cluster is chosen by looking at Table I. Similarly for the other columns of Table II. Our goal is to find the minimum number of clusters to be handled by robust analysis, in order to limit the computational burden. This goal is then achieved by exploiting either the NDVI or the γ metric because, for these metrics, the quality index in Table II increases faster with the number of selected clusters: we see that the selection of a single cluster is sufficient in the case of QB Trento data set, while two clusters need robust analysis for the WorldView data set.

Having recognized in NDVI and γ the most sensible metrics, we can focus on the selection of the number of clusters to be handled by using robust estimators. This is done by comparing the values in Table I with a threshold. If these values are greater than the threshold, a robust regression (either RO or BR) is exploited. Otherwise, an OLS estimator is considered. After many tests on different data sets over a variety of landscapes, the threshold is set to 0.5 for the NDVI metric and is set to 0.18 for the γ metric. The results of the analysis are reported in Table III, where we also give the results obtained by using the β metric (threshold set to 1.5) for completeness.

Table III makes clear the benefits of adopting a robust analysis to estimate the injection coefficients in a selected subset of clusters. In particular, we see that the proposed GLP-BR outperforms both the proposed GLP-RO and the state-of-the-art GLP-LS, which attains the worst performance among the three GLP-based approaches. The superiority of GLP-BR over GLP-RO comes with no surprise recalling that the former is more computationally demanding — a point that we further discuss later on. Comparable results for the three approaches are obtained only in the urban scenario acquired by the WV-3 sensor, where the robust regression is not needed.

On the contrary, a meaningful degradation in performance is measured by the quality indexes on both the QB Trento and the WV-4 Alice data sets where we note a reduction of 1% of the overall quality metric $Q2^n$. This can be explained by noting that these two data sets are more vegetated with respect to the urban Rio data set, as also confirmed by the values of NDVI reported in Table I. A further analysis is performed in Fig. 5, where the injection coefficients for the GLP-LS, the GLP-RO, and the GLP-BR using the NDVI cluster selection strategy are shown for all the spectral bands of the QB sensor. It is clearly seen that the main difference in the injection coefficients of the three methods is where vegetated areas are considered (see the right part from top to bottom in the maps of Fig. 5). This leads to one key conclusion of our analysis—the necessity of implementing robust regression algorithms for the injection coefficients when rural/vegetated areas have to be considered in the fusion problem. Along the same line, Table III also shows that the proposed GLP-BR and GLP-RO always outperform the benchmark approaches that are state of the art among pansharpening approaches.

These numerical results are also corroborated by the visual inspection of the fused products in Fig. 6, where some close-ups of the pansharpened products for the QB Trento data set are shown using a true color composition. Fig. 6 clearly shows a better rendering (closer to GT) of the vegetated area for the GLP-BR, with respect to the outcomes provided by the other approaches used as the benchmark.

E. FR Performance Assessment

This section addresses the validation at FR, in which case, due to the lack of a GT reference image, accurate indexes for performance assessment are not available. For the FR validation, we refer to the HQNR index. Table IV reports

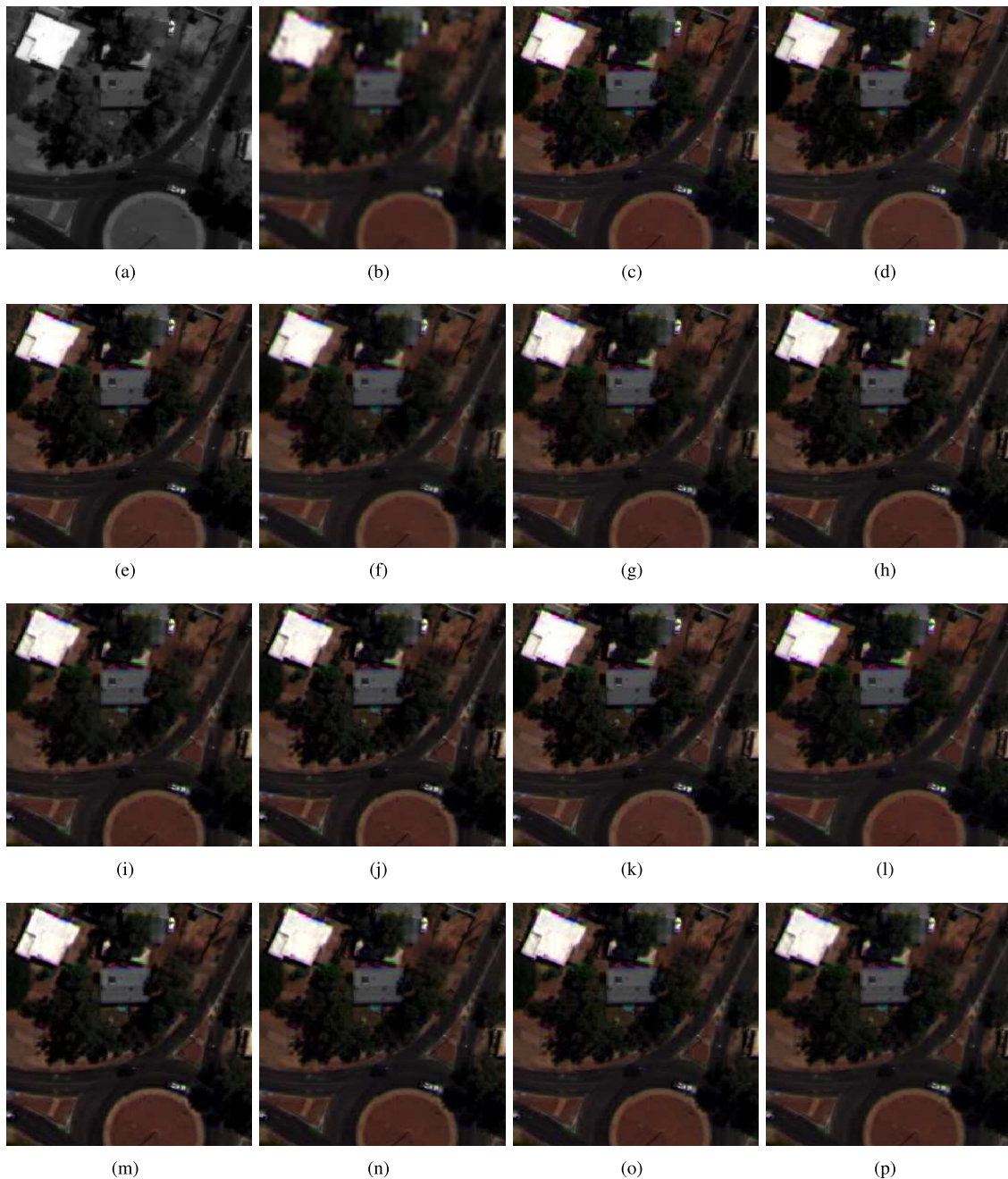


Fig. 7. Close-ups of the fusion results for the FR WV-4 Alice data set (selected bands: red, green, and blue). (a) PAN. (b) EXP. (c) BSDS. (d) GS. (e) GSA. (f) PRACS. (g) SFIM. (h) ATWT. (i) AWLP. (j) GLP-CBD. (k) C-GSA. (l) C-BSDS. (m) MF. (n) GLP-LS. (o) GLP-RO γ . (p) GLP-BR γ .

the outcomes of the benchmark approaches on the two FR data sets (i.e., QB Trento and WV-4 Alice), using the same threshold values as in Section V-D for the different selection strategies. The results corroborate those obtained at reduced resolution. According to HQNR, the best performance is obtained by the GLP-BR followed by the GLP-RO and the state-of-the-art GLP-LS. All other benchmark methods achieve lower performance.

Finally, Fig. 7 shows the pansharpened products on the WV-4 Alice FR data set for all the tested methods. It is worth noting the good balance between the spatial and spectral consistencies of the GLP-BR fused product, which is in agreement with the

quantitative results obtained by the D_S and the D_λ indexes in Table IV.

F. Computational Analysis

An important point of the experimental analysis is the evaluation of the computational burden of the proposed algorithms. Recall that the proposed pansharpening strategy encompasses a method to detect the clusters for which a computationally demanding robust regression is implemented. Table V reports the number q of clusters for which the robust estimation of the injection coefficients is implemented. The best selection

TABLE V

NUMBER $q \leq k$ OF CLUSTERS PROCESSED BY ROBUST REGRESSION, FOR THE DIFFERENT CLUSTER SELECTION STRATEGIES PRESENTED IN SECTION IV-B. THE DESIGN PARAMETERS ARE AS FOLLOWS: $k = 3$, NDVI-THRESHOLD SET TO 0.5, β -THRESHOLD SET TO 1.5, AND γ -THRESHOLD SET TO 0.18. BEST RESULTS FOR EACH DATA SET ARE SHOWN IN BOLDFACE. THE RELATED QUALITY ASSESSMENT IS REPORTED IN TABLE III FOR THE REDUCED RESOLUTION TEST CASES (i.e., WV-4 ALICE, WV-3 RIO, AND QB TRENTO) AND IN TABLE IV FOR THE FR TEST CASES (i.e., QB TRENTO FR AND WV-4 ALICE FR)

dataset	cluster selection	q
WV-4 Alice	NDVI	2
	β	2
	γ	2
WV-3 Rio	NDVI	0
	β	3
	γ	3
QB Trento	NDVI	1
	β	1
	γ	2
QB Trento FR	NDVI	1
	β	2
	γ	2
WV-4 Alice FR	NDVI	0
	β	3
	γ	3

TABLE VI

EXECUTION TIMES OF THE PANSHARPENING ALGORITHMS FOR THE WV-4 ALICE FR DATA SET, RUN OVER AN INTEL(R) CORE(TM) i7-7700HQ AT 2.80-GHZ PROCESSOR. DESIGN PARAMETERS ARE: $k = 3$, NDVI-THRESHOLD SET TO 0.5, β -THRESHOLD SET TO 1.5, AND γ -THRESHOLD SET TO 0.18. THE LAST COLUMN SHOWS THE INCREMENT OF THE COMPUTATIONAL TIME OF THE PROPOSED APPROACHES WITH RESPECT TO THE STATE-OF-THE-ART GLP-LS METHOD

	regression	cluster selection	time [s]	increment	
GLP	LS		1.8	0%	
		RO	NDVI	2.2	22%
			β	2.5	39%
	γ		2.5	39%	
	BR	NDVI	3.9	117%	
		β	5.2	189%	
		γ	5.2	189%	

strategy is based on the NDVI index, which always selects the smaller number of clusters.

As a consequence, we expect that NDVI strategy requires the lowest computational burden. This is confirmed by Table VI, which reports the execution time for the pansharpening algorithm on the WV-4 Alice FR data set, using an Intel(R) Core(TM) i7-7700HQ at 2.80-GHz processor. The last column in Table VI shows the increment of the computational time of the proposed approach with respect to the baseline represented by the state-of-the-art GLP-LS method. Note that the highest computational burden is required by the GLP-BR followed by the GLP-RO and the GLP-LS. Inside each category, the NDVI strategy is the less computational demanding followed by the other two strategies based on the analysis of residuals.

The additional computational burdens shown in Table VI do not appear unreasonable, especially when faced against the corresponding performance improvements discussed in the

previous sections. In summary, taking into account both the computational costs and the performance analysis, we conclude that the option providing the best tradeoff between the two contrasting requirements is represented by the GLP-BR exploiting the semantic-based (NDVI) strategy.

VI. CONCLUSION

Many of the Earth images collected by satellite sensors that we encounter in practical applications underwent a refinement process known as pansharpening, which refers to the bulk of image processing techniques designed to combine PAN images and MS images of the same illuminated scene, to obtain a final product with both high spatial resolution and richness of spectral content.

Due to the ubiquitousness of remotely sensed images in our everyday life (not to mention the many specialized advanced applications), the practical impact implied by any performance improvement over the existing pansharpening methods may be dramatic. In this article, we propose a pansharpening tool especially suited to illuminated scenes containing vegetated areas, which proves to outperform the state-of-the-art approaches at the cost of a limited additional computational burden.

We elaborate on the popular and top-performing context-based GLP algorithm based on the OLS regression-based injection model. The motivation of our work comes from the observation that the LS estimation of the injection coefficients may fail in the presence of non-Gaussian residuals typical, among others, of an illuminated scene with an abundance of vegetated areas. When the LS procedure performs poorly, the adoption of more sophisticated robust techniques is advisable, and we accordingly propose several context-based GLP approaches based on the framework of the M -estimators. We exploit the k -means algorithm to segment the MS image into homogeneous clusters, and three different strategies (one semantic-based and two based on the analysis of the residuals) to select which of these clusters need to be processed by robust regression. Two such regressions are considered, which are referred to as bisquare and RO.

We have conducted extensive experimental studies over several real-world data sets and a wide variety of landscapes. The experimental results show that the proposed pansharpening algorithms outperform the state-of-the-art approaches. In particular, the bottom line of our study is that the best trade-off between performance improvement and the unavoidable additional computational burden is represented by a semantic-based cluster selection strategy based on the NDVI index, combined with the bisquare robust estimation of the injection coefficients. We recommend the adoption of this pansharpening tool when the illuminated scene might contain a nonnegligible portion of vegetated areas.

REFERENCES

- [1] G. Vivone *et al.*, "A critical comparison among pansharpening algorithms," *IEEE Trans. Geosci. Remote Sens.*, vol. 53, no. 5, pp. 2565–2586, May 2015.
- [2] C. Thomas, T. Ranchin, L. Wald, and J. Chanussot, "Synthesis of multispectral images to high spatial resolution: A critical review of fusion methods based on remote sensing physics," *IEEE Trans. Geosci. Remote Sens.*, vol. 46, no. 5, pp. 1301–1312, May 2008.

- [3] H. Ghassemian, "A review of remote sensing image fusion methods," *Inf. Fusion*, vol. 32, pp. 75–89, Nov. 2016.
- [4] S. Li, X. Kang, L. Fang, J. Hu, and H. Yin, "Pixel-level image fusion: A survey of the state of the art," *Inf. Fusion*, vol. 33, pp. 100–112, Jan. 2017.
- [5] L. Alparone, B. Aiazzi, S. Baronti, and A. Garzelli, *Remote Sensing Image Fusion*. Boca Raton, FL, USA: CRC Press, 2015.
- [6] L. Alparone, L. Wald, J. Chanussot, C. Thomas, P. Gamba, and L. M. Bruce, "Comparison of pansharpening algorithms: Outcome of the 2006 GRS-S data-fusion contest," *IEEE Trans. Geosci. Remote Sens.*, vol. 45, no. 10, pp. 3012–3021, Oct. 2007.
- [7] P. S. Chavez, Jr., S. C. Sides, and J. A. Anderson, "Comparison of three different methods to merge multiresolution and multispectral data: Landsat TM and SPOT panchromatic," *Photogramm. Eng. Remote Sens.*, vol. 57, no. 3, pp. 295–303, Mar. 1991.
- [8] T.-M. Tu, S.-C. Su, H.-C. Shyu, and P. S. Huang, "A new look at IHS-like image fusion methods," *Inf. Fusion*, vol. 2, no. 3, pp. 177–186, Sep. 2001.
- [9] C. A. Laben and B. V. Brower, "Process for enhancing the spatial resolution of multispectral imagery using pan-sharpening," U.S. Patent 6011875, Jan. 4, 2000.
- [10] B. Aiazzi, S. Baronti, and M. Selva, "Improving component substitution pansharpening through multivariate regression of MS+pan data," *IEEE Trans. Geosci. Remote Sens.*, vol. 45, no. 10, pp. 3230–3239, Oct. 2007.
- [11] J. Choi, K. Yu, and Y. Kim, "A new adaptive component-substitution-based satellite image fusion by using partial replacement," *IEEE Trans. Geosci. Remote Sens.*, vol. 49, no. 1, pp. 295–309, Jan. 2011.
- [12] A. Garzelli, F. Nencini, and L. Capobianco, "Optimal MMSE pan sharpening of very high resolution multispectral images," *IEEE Trans. Geosci. Remote Sens.*, vol. 46, no. 1, pp. 228–236, Jan. 2008.
- [13] J. Nunez, X. Otazu, O. Fors, A. Prades, V. Pala, and R. Arbiol, "Multiresolution-based image fusion with additive wavelet decomposition," *IEEE Trans. Geosci. Remote Sens.*, vol. 37, no. 3, pp. 1204–1211, May 1999.
- [14] B. Aiazzi, L. Alparone, S. Baronti, and A. Garzelli, "Context-driven fusion of high spatial and spectral resolution images based on over-sampled multiresolution analysis," *IEEE Trans. Geosci. Remote Sens.*, vol. 40, no. 10, pp. 2300–2312, Jan. 2002.
- [15] L. Alparone, S. Baronti, B. Aiazzi, and A. Garzelli, "Spatial methods for multispectral pansharpening: Multiresolution analysis demystified," *IEEE Trans. Geosci. Remote Sens.*, vol. 54, no. 5, pp. 2563–2576, May 2016.
- [16] J. G. Liu, "Smoothing filter-based intensity modulation: A spectral preserve image fusion technique for improving spatial details," *Int. J. Remote Sens.*, vol. 21, no. 18, pp. 3461–3472, Jan. 2000.
- [17] G. Vivone, R. Restaino, M. Dalla Mura, G. Licciardi, and J. Chanussot, "Contrast and error-based fusion schemes for multispectral image pansharpening," *IEEE Geosci. Remote Sens. Lett.*, vol. 11, no. 5, pp. 930–934, May 2014.
- [18] X. Otazu, M. González-Audicana, O. Fors, and J. Núñez, "Introduction of sensor spectral response into image fusion methods. Application to wavelet-based methods," *IEEE Trans. Geosci. Remote Sens.*, vol. 43, no. 10, pp. 2376–2385, Oct. 2005.
- [19] L. Alparone, A. Garzelli, and G. Vivone, "Intersensor statistical matching for pansharpening: Theoretical issues and practical solutions," *IEEE Trans. Geosci. Remote Sens.*, vol. 55, no. 8, pp. 4682–4695, Aug. 2017.
- [20] G. Vivone, R. Restaino, and J. Chanussot, "Full scale regression-based injection coefficients for panchromatic sharpening," *IEEE Trans. Image Process.*, vol. 27, no. 7, pp. 3418–3431, Jul. 2018.
- [21] G. Vivone, R. Restaino, and J. Chanussot, "A regression-based high-pass modulation pansharpening approach," *IEEE Trans. Geosci. Remote Sens.*, vol. 56, no. 2, pp. 984–996, Feb. 2018.
- [22] R. Restaino, G. Vivone, M. Dalla Mura, and J. Chanussot, "Fusion of multispectral and panchromatic images based on morphological operators," *IEEE Trans. Image Process.*, vol. 25, no. 6, pp. 2882–2895, Jun. 2016.
- [23] G. Vivone, P. Adesso, R. Restaino, M. Dalla Mura, and J. Chanussot, "Pansharpening based on deconvolution for multiband filter estimation," *IEEE Trans. Geosci. Remote Sens.*, vol. 57, no. 1, pp. 540–553, Jan. 2019.
- [24] B. Aiazzi, S. Baronti, F. Lotti, and M. Selva, "A comparison between global and context-adaptive pansharpening of multispectral images," *IEEE Geosci. Remote Sens. Lett.*, vol. 6, no. 2, pp. 302–306, Apr. 2009.
- [25] B. Luo, M. M. Khan, T. Bienvenu, J. Chanussot, and L. Zhang, "Decision-based fusion for pansharpening of remote sensing images," *IEEE Geosci. Remote Sens. Lett.*, vol. 10, no. 1, pp. 19–23, Jan. 2013.
- [26] A. Garzelli, "Pansharpening of multispectral images based on nonlocal parameter optimization," *IEEE Trans. Geosci. Remote Sens.*, vol. 53, no. 4, pp. 2096–2107, Apr. 2015.
- [27] R. Restaino, M. Dalla Mura, G. Vivone, and J. Chanussot, "Context-adaptive pansharpening based on image segmentation," *IEEE Trans. Geosci. Remote Sens.*, vol. 55, no. 2, pp. 753–766, Feb. 2017.
- [28] F. Palsson, J. R. Sveinsson, and M. O. Ulfarsson, "A new pansharpening algorithm based on total variation," *IEEE Geosci. Remote Sens. Lett.*, vol. 11, no. 1, pp. 318–322, Jan. 2014.
- [29] L.-J. Deng, G. Vivone, W. Guo, M. Dalla Mura, and J. Chanussot, "A variational pansharpening approach based on reproducible kernel Hilbert space and heaviside function," *IEEE Trans. Image Process.*, vol. 27, no. 9, pp. 4330–4344, Sep. 2018.
- [30] G. Masi, D. Cozzolino, L. Verdoliva, and G. Scarpa, "Pansharpening by convolutional neural networks," *Remote Sens.*, vol. 8, no. 7, pp. 307–394, Jul. 2016.
- [31] Y. Wei, Q. Yuan, H. Shen, and L. Zhang, "Boosting the accuracy of multispectral image pansharpening by learning a deep residual network," *IEEE Geosci. Remote Sens. Lett.*, vol. 14, no. 10, pp. 1795–1799, Oct. 2017.
- [32] Q. Yuan, Y. Wei, X. Meng, H. Shen, and L. Zhang, "A multiscale and multidepth convolutional neural network for remote sensing imagery pan-sharpening," *IEEE J. Sel. Topics Appl. Earth Observ. Remote Sens.*, vol. 11, no. 3, pp. 978–989, Mar. 2018.
- [33] L. He *et al.*, "Pansharpening via detail injection based convolutional neural networks," *IEEE J. Sel. Topics Appl. Earth Observ. Remote Sens.*, vol. 12, no. 4, pp. 1188–1204, Apr. 2019.
- [34] D. Fasbender, J. Radoux, and P. Bogaert, "Bayesian data fusion for adaptable image pansharpening," *IEEE Trans. Geosci. Remote Sens.*, vol. 46, no. 6, pp. 1847–1857, Jun. 2008.
- [35] F. Fang, F. Li, C. Shen, and G. Zhang, "A variational approach for pansharpening," *IEEE Trans. Image Process.*, vol. 22, no. 7, pp. 2822–2834, Jul. 2013.
- [36] S. Li and B. Yang, "A new pan-sharpening method using a compressed sensing technique," *IEEE Trans. Geosci. Remote Sens.*, vol. 49, no. 2, pp. 738–746, Feb. 2011.
- [37] C. Jiang, H. Zhang, H. Shen, and L. Zhang, "A practical compressed sensing-based pan-sharpening method," *IEEE Geosci. Remote Sens. Lett.*, vol. 9, no. 4, pp. 629–633, Jul. 2012.
- [38] X. X. Zhu and R. Bamler, "A sparse image fusion algorithm with application to pan-sharpening," *IEEE Trans. Geosci. Remote Sens.*, vol. 51, no. 5, pp. 2827–2836, May 2013.
- [39] M. R. Vicinanza, R. Restaino, G. Vivone, M. Dalla Mura, and J. Chanussot, "A pansharpening method based on the sparse representation of injected details," *IEEE Geosci. Remote Sens. Lett.*, vol. 12, no. 1, pp. 180–184, Jan. 2015.
- [40] X. Meng, H. Shen, H. Li, L. Zhang, and R. Fu, "Review of the pansharpening methods for remote sensing images based on the idea of meta-analysis: Practical discussion and challenges," *Inf. Fusion*, vol. 46, pp. 102–113, Mar. 2019.
- [41] X. X. Zhu, C. Grohnfeldt, and R. Bamler, "Exploiting joint sparsity for pansharpening: The J-SparseFI algorithm," *IEEE Trans. Geosci. Remote Sens.*, vol. 54, no. 5, pp. 2664–2681, May 2016.
- [42] P. J. Huber, "Robust statistics," in *International Encyclopedia of Statistical Science*. Hoboken, NJ, USA: Wiley, 2011, pp. 1248–1251.
- [43] G. Vivone, "Robust band-dependent spatial-detail approaches for panchromatic sharpening," *IEEE Trans. Geosci. Remote Sens.*, vol. 57, no. 9, pp. 6421–6433, Sep. 2019.
- [44] L. Wald, T. Ranchin, and M. Mangolini, "Fusion of satellite images of different spatial resolutions: Assessing the quality of resulting images," *Photogramm. Eng. Remote Sens.*, vol. 63, no. 6, pp. 691–699, Jun. 1997.
- [45] B. Aiazzi, L. Alparone, S. Baronti, R. Carli, A. Garzelli, and L. Santurri, "Full scale assessment of pansharpening methods and data products," *Proc. SPIE*, vol. 9244, Oct. 2014, Art. no. 924402.

- [46] B. Aiuzzi, L. Alparone, S. Baronti, A. Garzelli, and M. Selva, "MTF-tailored multiscale fusion of high-resolution MS and pan imagery," *Photogramm. Eng. Remote Sens.*, vol. 72, no. 5, pp. 591–596, May 2006.
- [47] N. R. Draper and H. Smith, *Applied Regression Analysis*, 3rd ed. Hoboken, NJ, USA: Wiley, 1998.
- [48] J. Fox, "Robust regression: An R and S-plus companion to applied regression," MDPI Remote Sens., Univ. Salerno, Salerno, Italy, Tech. Rep., 2002.
- [49] P. S. Chavez, "An improved dark-object subtraction technique for atmospheric scattering correction of multispectral data," *Remote Sens. Environ.*, vol. 24, no. 3, pp. 459–479, Apr. 1988.
- [50] A. Garzelli, B. Aiuzzi, L. Alparone, S. Lolli, and G. Vivone, "Multispectral pansharpening with radiative transfer-based detail-injection modeling for preserving changes in vegetation cover," *Remote Sens.*, vol. 10, no. 8, p. 1308, Aug. 2018.
- [51] R. A. Schowengerdt, *Remote Sensing: Models and Methods for Image Processing*, 3rd ed. Orlando, FL, USA: Elsevier, 2007.
- [52] S. Kotz, N. Balakrishnan, and N. L. Johnson, *Continuous Multivariate Distributions*, vol. 1. Hoboken, NJ, USA: Wiley, 2004.
- [53] B. Aiuzzi, S. Baronti, M. Selva, and L. Alparone, "Bi-cubic interpolation for shift-free pan-sharpening," *ISPRS J. Photogram. Remote Sens.*, vol. 86, pp. 65–76, Dec. 2013.
- [54] A. Garzelli and F. Nencini, "Hypercomplex quality assessment of multi/hyperspectral images," *IEEE Geosci. Remote Sens. Lett.*, vol. 6, no. 4, pp. 662–665, Oct. 2009.
- [55] L. Alparone, S. Baronti, A. Garzelli, and F. Nencini, "A global quality measurement of pan-sharpened multispectral imagery," *IEEE Geosci. Remote Sens. Lett.*, vol. 1, no. 4, pp. 313–317, Oct. 2004.
- [56] Z. Wang and A. C. Bovik, "A universal image quality index," *IEEE Signal Process. Lett.*, vol. 9, no. 3, pp. 81–84, Mar. 2002.
- [57] R. H. Yuhas, A. F. H. Goetz, and J. W. Boardman, "Discrimination among semi-arid landscape endmembers using the spectral angle mapper (SAM) algorithm," in *Proc. Summaries 3rd Annu. JPL Airborne Geosci. Workshop*, 1992, pp. 147–149.
- [58] L. Alparone, B. Aiuzzi, S. Baronti, A. Garzelli, F. Nencini, and M. Selva, "Multispectral and panchromatic data fusion assessment without reference," *Photogramm. Eng. Remote Sens.*, vol. 74, no. 2, pp. 193–200, Feb. 2008.



Gemine Vivone (Senior Member, IEEE) received the B.Sc. and M.Sc. degrees (*summa cum laude*), and the Ph.D. degree in information engineering from the University of Salerno, Fisciano, Italy, in 2008, 2011, and 2014, respectively.

In 2012, he was a Visiting Researcher with the North Atlantic Treaty Organization (NATO) Undersea Research Center, La Spezia, Italy. In 2013, he was also a Visiting Scholar with the Grenoble Institute of Technology (INPG), Grenoble, France. In 2014, he joined the NATO, Science and Technology Organization (STO), Center for Maritime Research and Experimentation (CMRE), La Spezia, as a Scientist. In 2019, he was also an Assistant Professor with the University of Salerno. He is currently a Researcher with the National Research Council, Rome, Italy. His main research interests focus on statistical signal processing, detection of remotely sensed images, data fusion, and tracking algorithms.

Dr. Vivone received the Symposium Best Paper Award at the IEEE International Geoscience and Remote Sensing Symposium (IGARSS) in 2015 and the Best Reviewer Award from the IEEE TRANSACTIONS ON GEOSCIENCE AND REMOTE SENSING in 2017. He serves as a referee for several remote sensing and image processing journals. He was the Lead Guest Associate Editor of a Special Stream of the IEEE GEOSCIENCE AND REMOTE SENSING LETTERS, a Guest Associate Editor of a Special Issue of *MDPI Remote Sensing* and a Co-Editor of a Special Issue of *International Journal of Image and Data Fusion*. He is also an Associate Editor of the IEEE GEOSCIENCE AND REMOTE SENSING LETTERS (GRSL) and an Editorial Board Member of *MDPI Remote Sensing*.



Stefano Marano (Senior Member, IEEE) received the Laurea degree (Hons.) in electronic engineering and the Ph.D. degree in electronic engineering and computer science from the University of Naples, Naples, Italy, in 1993 and 1997, respectively.

Since 1999, he has been with the University of Salerno, Fisciano, Italy, where he is currently a Professor with the Department of Information and Electrical Engineering, and Applied Mathematics (DIEM). He has held visiting positions at the Physics Department, College of Cardiff, University of Wales,

Cardiff, U.K., and the Department of Electrical and Computer Engineering, University of California at San Diego, San Diego, CA, USA, in 1996 and 2013, respectively. His areas of interest include statistical signal processing with an emphasis on distributed inference, sensor networks, and information theory. In these areas, he has published about 180 articles, including some invited, on leading international journals/transactions (about 80) and proceedings of leading international conferences.

Dr. Marano received the Best Paper Award for the IEEE TRANSACTIONS ON ANTENNAS AND PROPAGATION in 1999 for his work on stochastic modeling of electromagnetic propagation in urban environments. He also coauthored the article for which he received the Best Student Paper Award (Second Place) at the 12th Conference on Information Fusion in 2009. He was in the Organizing Committee of the Ninth International Conference on Information Fusion (FUSION 2006) and the 2008 IEEE Radar Conference (RADARCON 2008). He is also the Subcommittee Chair of the EURASIP Special Area Team TMTSP SAT. He is also the Guest Editor of the Special Issue on Distributed and Centralized Estimation in Wireless Sensor Networks of *EURASIP Journal on Advances in Signal Processing*. He served as an Associate Editor for the IEEE TRANSACTIONS ON SIGNAL PROCESSING from 2010 to 2014 and as an Associate Editor and a Technical Editor for the IEEE TRANSACTIONS ON AEROSPACE AND ELECTRONIC SYSTEMS from 2009 to 2016.



Jocelyn Chanussot (Fellow, IEEE) received the M.Sc. degree in electrical engineering from the Grenoble Institute of Technology (Grenoble INP), Grenoble, France, in 1995, and the Ph.D. degree from the Université de Savoie, Annecy, France, in 1998.

From 2015 to 2017, he was a Visiting Professor with the University of California at Los Angeles (UCLA), Los Angeles, CA, USA. He was a member of the Institut Universitaire de France from 2012 to 2017. He has been a Visiting Scholar with Stanford University, Stanford, CA, USA; KTH, Stockholm, Sweden; and the National University of Singapore (NUS), Singapore. Since 2013, he has also been an Adjunct Professor with the University of Iceland, Reykjavik, Iceland. He holds the AXA Chair in remote sensing and also an Adjunct Professor with the Chinese Academy of Sciences, Aerospace Information research Institute, Beijing, China. Since 1999, he has been with Grenoble INP, where he is currently a Professor of signal and image processing. His research interests include image analysis, hyperspectral remote sensing, data fusion, machine learning, and artificial intelligence.

Dr. Chanussot was a member of the Machine Learning for Signal Processing Technical Committee of the IEEE Signal Processing Society from 2006 to 2008. He was the founding President of the IEEE Geoscience and Remote Sensing Society (GRS-S) French Chapter from 2007 to 2010, for which he received the 2010 IEEE GRS-S Chapter Excellence Award. He has received multiple outstanding paper awards. He was the Vice-President of the IEEE Geoscience and Remote Sensing Society, in charge of meetings and symposia, from 2017 to 2019. He was the General Chair of the first IEEE GRS-S Workshop on Hyperspectral Image and Signal Processing, Evolution in Remote sensing (WHISPERS). He was the Chair and the Co-Chair of the GRS-S Data Fusion Technical Committee from 2005 to 2008 and from 2009 to 2011, respectively. He was also the Program Chair of the IEEE International Workshop on Machine Learning for Signal Processing in 2009. He was the Editor-in-Chief of the IEEE JOURNAL OF SELECTED TOPICS IN APPLIED EARTH OBSERVATIONS AND REMOTE SENSING from 2011 to 2015. In 2014, he served as a Guest Editor for the *IEEE Signal Processing Magazine*. He is also an Associate Editor of the IEEE TRANSACTIONS ON GEOSCIENCE AND REMOTE SENSING, the IEEE TRANSACTIONS ON IMAGE PROCESSING, and the PROCEEDINGS OF THE IEEE. He was a Highly Cited Researcher (Clarivate Analytics/Thomson Reuters) from 2018 to 2019.